Analytica Chimica Acta 1202 (2022) 339689

Contents lists available at ScienceDirect

Analytica Chimica Acta

journal homepage: www.elsevier.com/locate/aca

Molecularly imprinted Ni-polyacrylamide-based electrochemical sensor for the simultaneous detection of dopamine and adenine

Tianrun Zhang [a], Xiuwei Xuan [a, **], Mingji Li [a, *], Cuiping Li [a], Penghai Li [a], Hongji Li [b, ***]

[a] Tianjin Key Laboratory of Film Electronic and Communication Devices, Engineering Research Center of Optoelectronic Devices & Communication Technology (Ministry of Education), School of Integrated Circuit Science and Engineering, Tianjin University of Technology, Tianjin, 300384, PR China
[b] Tianjin Key Laboratory of Organic Solar Cells and Photochemical Conversion, Tianjin Key Laboratory of Drug Targeting and Bioimaging, School of Chemistry and Chemical Engineering, Tianjin University of Technology, Tianjin, 300384, PR China

HIGHLIGHTS

- An Ni-polyacrylamide(PAM)-MIP matrix is electro-polymerized in situ.
- The MIP sensor responds simultaneously to dopamine (DA) and adenine (Ade).
- The morphology of Ni-PAM-MIP before and after template removal is observed.
- A series of quantitative models is established in the wide range of pH 5.0–9.0
- The dual-MIP sensor has excellent selectivity and stability for the assay of DA and Ade.

GRAPHICAL ABSTRACT

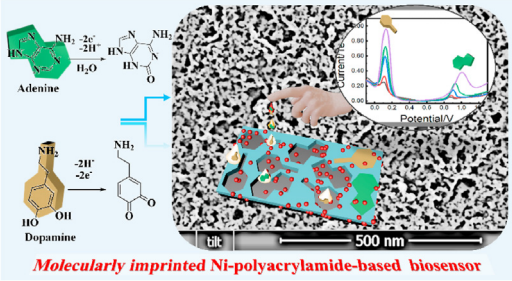

ARTICLE INFO

Article history:
Received 22 November 2021
Received in revised form
29 January 2022
Accepted 4 March 2022
Available online 7 March 2022

Keywords:
Electrochemical biosensor
Molecularly imprinted polymers
Dopamine
Adenine
Electrodeposition

ABSTRACT

Molecularly imprinted polymer (MIP) membranes prepared in situ present several advantages: they maintain the original morphology, adhere strongly to the collector, and exhibit a controllable structure. In this study, a Ni-polyacrylamide (PAM)-MIP matrix was fabricated in situ on glassy carbon via the one-step electro-polymerization of AM monomers in the presence of Ni and template molecules. Ni^{2+} ions were introduced as oxidants to promote AM polymerization and bulking agents to fabricate a three-dimensional porous PAM-MIP matrix. The Ni-PAM-based MIP sensor exhibited a quantitative dual response toward dopamine (DA) and adenine (Ade) in the pH range of 5.0–9.0. The linear concentration range changed depending on the pH environment, and the concentrations of DA and Ade ranged from 0.6 to 200 μM and from 0.4 to 300 μM, respectively. The ranges of detection limits (S/N = 3) were 0.12–0.37 μM for DA and 0.15–0.36 μM for Ade. In addition, the dual-MIP sensor exhibited high reliability in the detection of DA and Ade in human serum owing to its excellent anti-interference ability and long-term stability. The technique developed in this study is expected to facilitate the construction of multi-target response electrochemical biosensors and the reliable determination of small molecules with high selectivity and stability.

* Corresponding author. .
** Corresponding author. .
*** Corresponding author.
E-mail addresses: xiuweixuan@tju.edu.cn (X. Xuan), limingji@163.com (M. Li), hongjili@yeah.net (H. Li).

https://doi.org/10.1016/j.aca.2022.339689
0003-2670/

1. Introduction

Dopamine (DA) and adenine (Ade) are nitrogen-containing organic compounds coexisting in physiological body fluids including blood, urine, and cytoplasm, are used as biomarkers for diseases affecting the nervous and immune systems [1,2]. DA is a key neurotransmitter in the human brain; however, its presence at abnormal concentrations in the body can lead to various neurological disorders, such as Parkinson's disease, epilepsy, schizophrenia, and Tourette syndrome [3–5]. Ade is a component of deoxyribonucleic acid (DNA) and ribonucleic acid (RNA) that plays important roles in neurotransmitter release, metabolic regulation, and coenzyme formation; its presence at anomalous concentrations is related to conditions such as AIDS, cancer, Parkinson's disease, and epilepsy [6–9]. Therefore, the development of rapid and accurate methods for the detection of DA and Ade in complex physiological environments is essential for monitoring human health and early detection of various diseases.

To date, many different techniques have been successfully applied to detect DA and Ade, including chromatography, fluorescence spectrometry, chemiluminescence analysis, and electrochemical assays [10–15]. In particular, electrochemical methods are the most convenient, simple, and rapid; furthermore, they are suitable for the fabrication of inexpensive universal medical instruments. Both DA and Ade are electroactive compounds; however, DA has a lower oxidation potential and stronger electrochemical activity than Ade. In terms of trace detection of DA, electrochemical analysis has significant advantages over other methods, which supports the development of numerous modified electrodes, as reported in the literature [16–19]. In addition, various modifiers such as graphene [14], MoS_2 [6,10], metal-organic framework@carbon nanotube (CNT) [20], 1-docosyloxylmethylpyrene/semiconducting single-walled CNTs [21], and polyimidazole/graphene oxide [2] have been used for the determination of Ade. The electrochemical determination of Ade is based on the electrooxidation of purine bases at the 2- and 8-positions [22,23]. Owing to the different electrocatalytic activities of various modifiers, the electrochemical reaction pathways or oxidation products of Ade are different, which alters the sensing performance. As there are multiple reaction sites and paths of Ade, the concentrations of DA and Ade can be measured synchronously without mutual interference, thereby increasing the reliability of the detection results.

However, traditional electrochemical sensors suffer from low stability, reproducibility, and solidity. Preventing environmental contamination and differences between samples in the manufacturing and application processes is difficult for such sensors. Molecularly imprinted polymer (MIP) sensing membranes have attracted extensive attention in recent years as a possible solution to these problems [24–26]. MIP technology is based on the fabrication of polymer network matrices using various methods, whereby a large number of highly specific binding sites are introduced through template molecules [27]. Conventional methods for preparing surface MIP structures include the polymerization of functional monomers, cross-linkers, and templates by covalent or noncovalent interactions, such as free-radical polymerization, sol-gel methods, and atom-transfer radical polymerization [17,28,29]. However, the MIP membranes obtained via these methods may contain residual surfactants and tend to precipitate out of the electrolyte. Additionally, the operational conditions for free-radical reactions are harsh. Furthermore, the electro-polymerization method can be used to fabricate MIP sensing films, which exhibit some characteristics of in-situ formation, and possess high solidity, stability, and process-repeatability as MIP membranes [24,30–32].

Polyacrylamide (PAM) is a biodegradable polymer characterized by non-toxicity, biocompatibility, film-forming ability, mechanical and chemical resistance, and high hydrophilicity. Therefore, PAM is a common functional material used in drug delivery, cell culture, and soil improvement [7,33,34]. The one-step synthesis of PAM-based nanocomposites embedded with various metal nanoparticles, such as Au and Ag, has already been reported in the literature. Inspired by such reports, we developed a novel system to promote the electro-polymerization of AM monomers under the typical conditions maintained during the electrochemical oxidation of biomolecules and reduction of metal ions. In this way, the synthesis of the metal nanoparticle-PAM matrix and the loading of template molecules on the collector can occur simultaneously.

The aim of this study was to fabricate a dual-MIP electrochemical sensor based on an Ni-PAM matrix to achieve the selective enrichment and reliable recognition of DA and Ade. To the best of our knowledge, this is the first report describing the electrodeposition of single- and double-response Ni-PAM-MIP sensing layers on a glassy carbon electrode (GCE) via the in-situ electro-polymerization of AM monomers assisted by Ni and template molecules. The valence of Ni, the morphology of Ni-PAM-MIP, and the concentration of the template molecules were controlled by adjusting the size and polarity of the step electrical signal. In this study, the possible mechanism of formation is hypothesized and discussed. Considering the pH difference between body fluids such as cytoplasm, blood, and urine, we established a quantitative model consisting of a series of linear regression equations over the wide pH range of 5.0–9.0. The as-prepared dual-MIP sensing electrode exhibited high sensitivity, excellent selectivity, and a reliable response toward DA and Ade.

2. Experimental section

2.1. Reagents and materials

DA, Ade, and uric acid (UA) were purchased from Alfa Aesar (China). Cytosine (Cyt), guanine (Gua), and thymine (Thy) were supplied by Shanghai Yuanye Bio-Technology Co., Ltd. (China). L-tyrosine (Tyr), L-serine (Ser), ascorbic acid (AA), and $CuCl_2{\bullet}2H_2O$ were supplied by the Tianjin Guangfu Fine Chemical Research Institute (China). Na_2HPO_4, NaH_2PO_4, KCl, NaCl, $NiCl_2$, $ZnCl_2$, $FeCl_2{\bullet}4H_2O$, glutamate (Glu), and AM were obtained from Tianjin Damao Chemical Reagent Factory (China). L-Tryptophan (Trp) was purchased from Aladdin Reagent Co., Ltd. (Shanghai). L-Lysine (Lys) was purchased from Shanghai Macklin Biochemical Co., Ltd. Absolute ethanol, $NaSO_4$, $CaCl_2$, and $NaSO_3$ were purchased from Tianjin Jiangtian Unified Technology Co., Ltd. (China). K_2CO_3 and $MgCl_2{\bullet}6H_2O$ were purchased from Tianjin Fortune Chemical Reagent Co., Ltd. (China). Human serum was purchased from Beijing Solarbio Technology Co., Ltd. (China). Glassy carbon sheets of dimensions 10 mm × 20 mm × 1 mm were purchased from Beijing Jingke Scientific Instrument Co., Ltd. Phosphate-buffered saline (PBS) solutions of differing pH (5.0–9.0) were prepared using 0.1 M Na_2HPO_4, 0.1 M NaH_2PO_4, and 0.1 M NaOH. All chemical reagents were used without further purification. Ultrapure water having a resistivity of 18.2 MΩ cm was used in all the experiments.

2.2. Preparation of molecularly imprinted sensing electrode

First, a mixed solution containing 1 mM AM, 1 mM $NiCl_2$, 0.5 mM DA, 0.5 mM Ade, and 0.05 M KCl was prepared. DA and Ade were used as the imprinting template molecules, whereas AM was the monomer from which the polymer matrix was derived. Thereafter, the GCE was polished to a mirror surface using Al_2O_3 polishing powder having a particle size of 0.05 μm and deerskin. The GCE was ultrasonically cleaned in 1:1 HNO_3, ultrapure water,

absolute ethanol, and ultrapure water in order for 10 min each, and dried using nitrogen prior to use. Subsequently, a three-electrode system consisting of a cleaned glassy carbon sheet as the working electrode (GCE), a Pt sheet as the counter electrode, and an Ag/AgCl electrode as the reference was fabricated. These electrodes were immersed in the aforementioned electrolyte at a height of 10 mm and then connected to an electrochemical workstation. The sensing layer was deposited using the double-potential-step method. In the first step, the potential and time were 2 V and 1 s, respectively, and in the second step, they were −0.6 V and 0.2 s, respectively. The deposition proceeded through 600 cycles (Scheme 1(a), Video S1). Finally, the three-electrode system was immersed in 0.1 M PBS having a pH of 7.4, and ten differential pulse voltammetry (DPV) curves were continuously scanned in the potential range of −0.2–1.4 V (Video S2, Fig. S1). In the PBS solution, the oxidation peaks of DA and Ade appeared in the initial DPV curve, which confirmed that the two analytes were distributed as template molecules in the Ni-PAM sensitive membrane. As the scanning time increased, the oxidation peaks of the two analytes gradually disappeared. This indicates that DA and Ade were removed from the GCE surfaces, and dual-MIP sensing electrodes were obtained. As a control, non-imprinted polymers (NIPs: Ni-PAM) were prepared using the same procedure in the absence of DA and Ade templates.

Supplementary video related to this article can be found at https://doi.org/10.1016/j.aca.2022.339689

To investigate the sensing mechanism, PAM, DA-MIP, and Ade-MIP sensing electrodes were prepared by applying the same process at different electrolyte compositions (Scheme 1(c)).

2.3. Apparatus

The morphologies and microstructures of the samples were characterized by field-emission scanning electron microscopy (FE-SEM; FEL, Verios 460 L USA; MERLIN Compact, Carl Zeiss, Germany) and atomic force microscopy (AFM; Dimension ICON, Bruker, Germany). The chemical compositions and bonding states were analyzed by X-ray photoelectron spectroscopy (XPS; Escalab 250Xi, Thermo Scientific, USA) and Fourier-transform infrared spectroscopy (FTIR; Tensor 27, Bruker, Germany).

Electrochemical measurements including DPV, electrochemical impedance spectroscopy (EIS), and cyclic voltammetry (CV) were performed using an electrochemical workstation (CHI660E, CHI1140C, Chenhua, Shanghai, China). The three-electrode system consisted of a modified GCE (immersion area: 1 cm^2) as the working electrode, an Ag/AgCl electrode as the reference, and a Pt-sheet auxiliary electrode. The peak currents obtained from the DPV

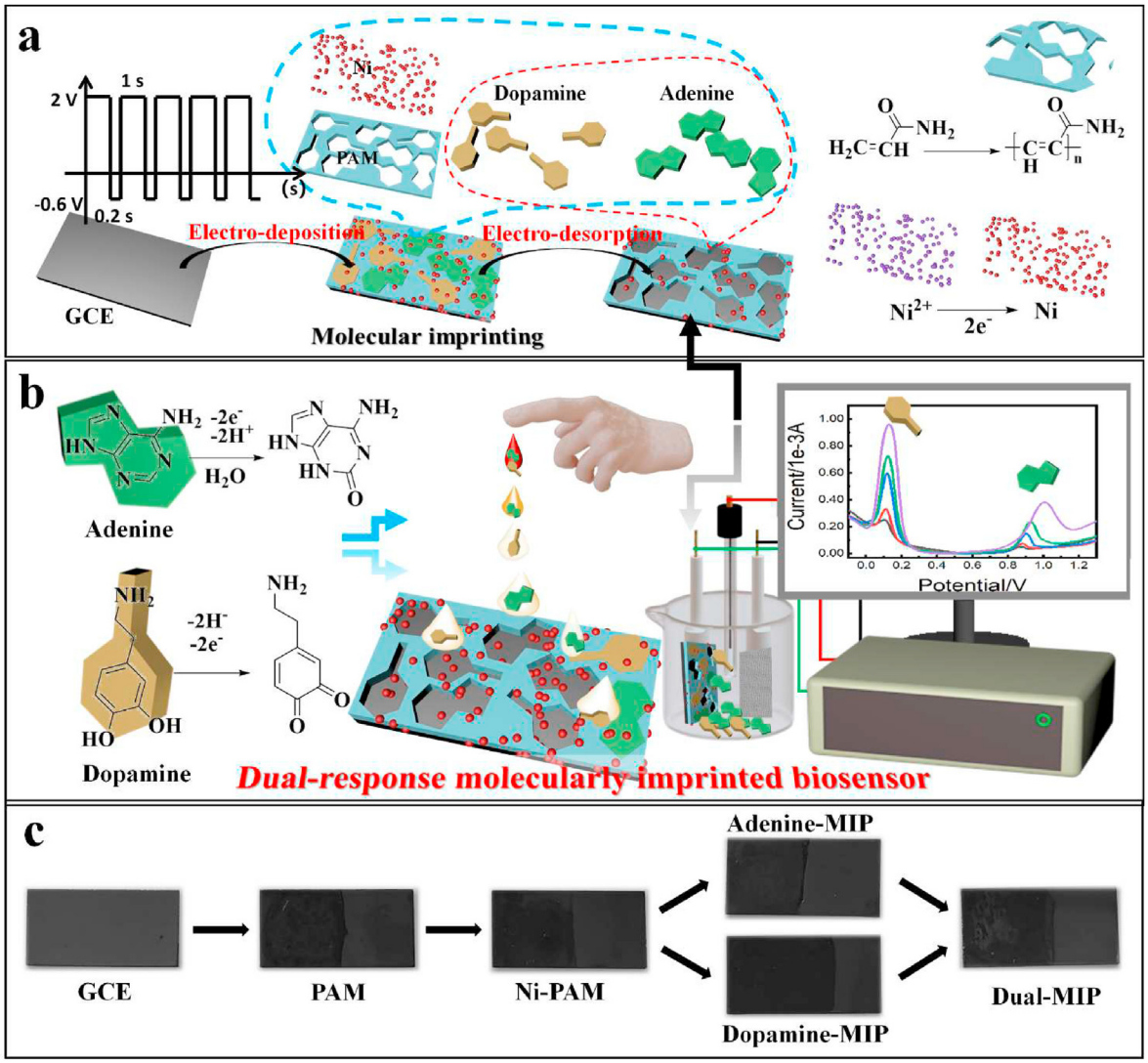

Scheme 1. (a) Assembly process of the dual-response MIP sensing membrane for dopamine (DA) and adenine (Ade). (b) Electrochemical response mechanism of DA and Ade.

curves were calculated after deducting the background current (Fig. S2).

3. Results and discussion

3.1. Formation mechanism of dual-MIP sensing film

We prepared the dual-MIP sensing film by applying a pulsed electric field of 2 V for 1 s and −0.6 V for 0.2 s to accomplish the electro-polymerization of AM (CH_2=$CHCONH_2$) monomers, electrostatic adsorption of Ade and DA, and electrodeposition of Ni nanoparticles in a single step. Under the action of the Ni^{2+}/DA (or Ade) redox initiator system, AM molecules were polymerized into PAM, a super-absorbent resin that can absorb a large amount of electrolyte. Therefore, the DA-Ade-Ni-PAM film was electrodeposited on the GCE surface. Scheme 1(a) describes the deposition mechanism. First, the electric field drove the coordination between Ni^{2+} and AM monomers [35]. Then, DA and Ade were oxidized at a positive potential of 2 V, whereas Ni^{2+} ions were reduced at a negative potential of −0.6 V ($Ni^{2+} + 2e^- \rightarrow Ni$). Subsequently, the polymerization of AM into PAM was initiated by DA and Ade acting as reducing agents and Ni^{2+} ions acting as oxidizing agents. To obtain the modified DA-Ade-Ni-PAM layer, the DA and Ade template molecules were released by exploiting the combined effects of electro-reduction and the volume expansion of PAM in the aqueous solution. Scheme 1(b) illustrates the possible oxidation reactions of DA and Ade on the dual-MIP electrode; Scheme 1(c) depicts photographs of GCE, PAM/GCE, Ni-PAM/GCE, and three MIP electrodes.

3.2. Characterization of the sensing electrodes

Fig. 1 and S3 show FE-SEM images of various electrodes. The GCE presented a smooth surface (Fig. S3), while the separate PAM layer was a dense and continuous film; the Ni nanoparticles improved the roughness of the sensitive layer (Fig. 1(a and b)). A comparison of the morphology of the Ni-PAM-Ade (Ade-MIP) film before and after the removal of Ade molecules highlights the formation of numerous holes following removal (Fig. 1(c and d)). In contrast, the Ni-PAM-DA (DA-MIP) film was significantly thicker than the Ni-PAM-Ade layer (Fig. 1(e)); this may be explained by the fact that DA molecules exhibit excellent polymerization and adhesion abilities. Fine DA-imprinted holes were observed following the removal of the adhering PDA layer (Fig. 1(f)). To endow the MIP sensor with the ability to synchronously detect DA and Ade, we also deposited an Ade-DA-Ni-PAM film on a GCE surface (Fig. 1(g)). Following the removal of the DA and Ade templates, we observed numerous imprinted holes (Fig. 1(h)). The filling effect of the imprinted holes on the dual-PAM sensor was also observed after employing it to detect a 5 mM DA solution (Fig. 1(i)). These results confirm the formation of a dual-MIP film for the detection of DA and Ade.

Fig. 2(a–e) shows the XPS profiles of the PAM/GCE, Ni-PAM/GCE, DA-MIP, Ade-MIP, and dual-MIP electrodes. The various sensing layers were composed of C, N, and O atoms. The C 1s core-level XPS profiles (Fig. 2(a)) of different sensing layers exhibited five peaks centered at 284.7, 286.1, 288.9, 293.1, and 295.9 eV, which were attributed to phenyl carbon (C=C/C–H), -C–CH_2–O/C–N, carbonyl carbon (C=O/O–C=O), O=C–N, and N–C=N bonds, respectively [36]. Comparing the C 1s spectrum of Ade-MIP with that of PAM, the intensities of the peaks attributed to the O=C–N bond at ~292.7 eV and the N–C=N bond at ~295.5 eV appeared significantly higher. These bonds belonged to the molecular structure of Ade, indicating the successful loading of a large number of Ade molecules on the sensing layer. In the spectrum of the cleaned Ade-MIP electrode, the peaks attributed to these two bonds disappeared, confirming the removal of Ade and the consequent formation of molecular imprints. Similarly, the formation and disappearance of the N–C=O peak were observed in the C 1s core-level spectra of the DA-MIP electrode before and after removing the template, respectively. In the spectra of the dual-MIP electrode, the intensity of the C=O peak increased upon loading the DA and Ade molecules and decreased following the removal of the oxidized templates.

According to the deconvolution of the N 1s core region (Fig. 2(b)), the peak at a binding energy of ~400 eV belonged to the –NH– group (C–N–C), while the one at ~401.7 eV may be attributed to the $-NH_2$ group (-C-NH_2). The peaks attributed to the –NH– (399.7 eV) and $-NH_2$ (401.2 eV) groups in the N 1s spectra of the Ni-PAM layer shifted toward lower binding energies following the adsorption of Ni^{2+}, probably because of an increase in the electron cloud density around the N atoms (N–O bond) [37]. Upon comparing the Ade-MIP spectra before and after template removal, we observed that the strength ratio of the C–N–C/-C-NH_2 bonds decreased, suggesting the introduction and subsequent elimination of Ade molecules. Similar changes were more evident in the spectra of the DA-MIP sensor before and after cleaning [38]. The O 1s spectrum of PAM could be deconvoluted into two peaks at the binding energies of 532.28 and 531.46 eV, which were assigned to the C–O/O–H/O–N and C=O groups, respectively [37]. Following the adsorption of Ni^{2+} ions, the C=O peak shifted toward higher binding energies: this was primarily attributed to a decrease in electron cloud density around the O atoms after bonding with Ni^{2+} ions [39]. Upon comparing the XPS profiles of various MIP electrodes before and after cleaning, we observed that the C=O bond content increased for Ade-MIP and decreased for the DA-MIP and dual-MIP layers. In addition, in the O 1s spectrum of the dual-MIP sensing electrode, the peak at the binding energy of 535.8 eV was attributed to the C–O moiety in ethers and esters, derived from the grafting reaction between DA and Ade [40]. The high-resolution Ni 2p spectrum of the dual-MIP sensor exhibited one peak at 848.6 eV, two spin-orbit splitting peaks at 855.8 (Ni $2p_{3/2}$) and 873.5 (Ni $2p_{1/2}$) eV, and two weak shake-up satellites at 861.8 and 879.0 eV, corresponding to Ni–N, metallic Ni, and Ni (II), respectively [41–43]. The peaks at 861.8 and 871.8 eV could be assigned to the coordination between Ni^{2+} ions and functional groups, which agrees with the changes in the O 1s and N 1s peaks in Ni-PAM following the metal ion adsorption. In the spectrum of the dual-MIP sensor, the Ni^0 peak intensity was weakened following the removal of DA and Ade owing to oxidation or removal of Ni.

Fig. 2(f) depicts the FTIR spectra of PAM, Ade-MIP, DA-MIP, and dual-MIP/GCEs recorded prior to the removal of Ade and DA. In the PAM spectrum, the absorption band observed at 3406 cm^{-1} may be attributed to –OH stretching vibrations of water adsorbed from the environment; the bands at 3201.6, 2931, 1668.3, and 1421 cm^{-1} corresponded to the stretching vibrations of N–H, $-CH_3$, amide –C=O, and methylene ($=CH_2$) groups, while the one at 1074 cm^{-1} pertained to the -C-N bending vibration [7,44–46]. The electro-adsorption of Ade molecules was confirmed by the observation of characteristic peaks at 1681 cm^{-1} for $-NH_2$, 1651 cm^{-1} for C=N, 1628 cm^{-1} for C=C, 1523 cm^{-1} for C–N, and 1238 cm^{-1} for C–N [47]. Similarly, the electro-adsorption of DA was confirmed by the appearance of novel peaks at 1718 cm^{-1} for carboxyl C=O, 1630 cm^{-1} for amide I, 1587 cm^{-1} for amide II (-N-H), 1460 cm^{-1} for C=N stretching, 1380 cm^{-1} for C–N–C, and 1180 cm^{-1} for C–O–H [38]. These results further confirm the successful introduction of template molecules during the formation of the Ni-PAM matrix.

3.3. Electrochemical properties of sensing electrodes

Fig. 3(a) shows the three-dimensional AFM images of the various electrodes. We compared the 3-D topography of the MIP

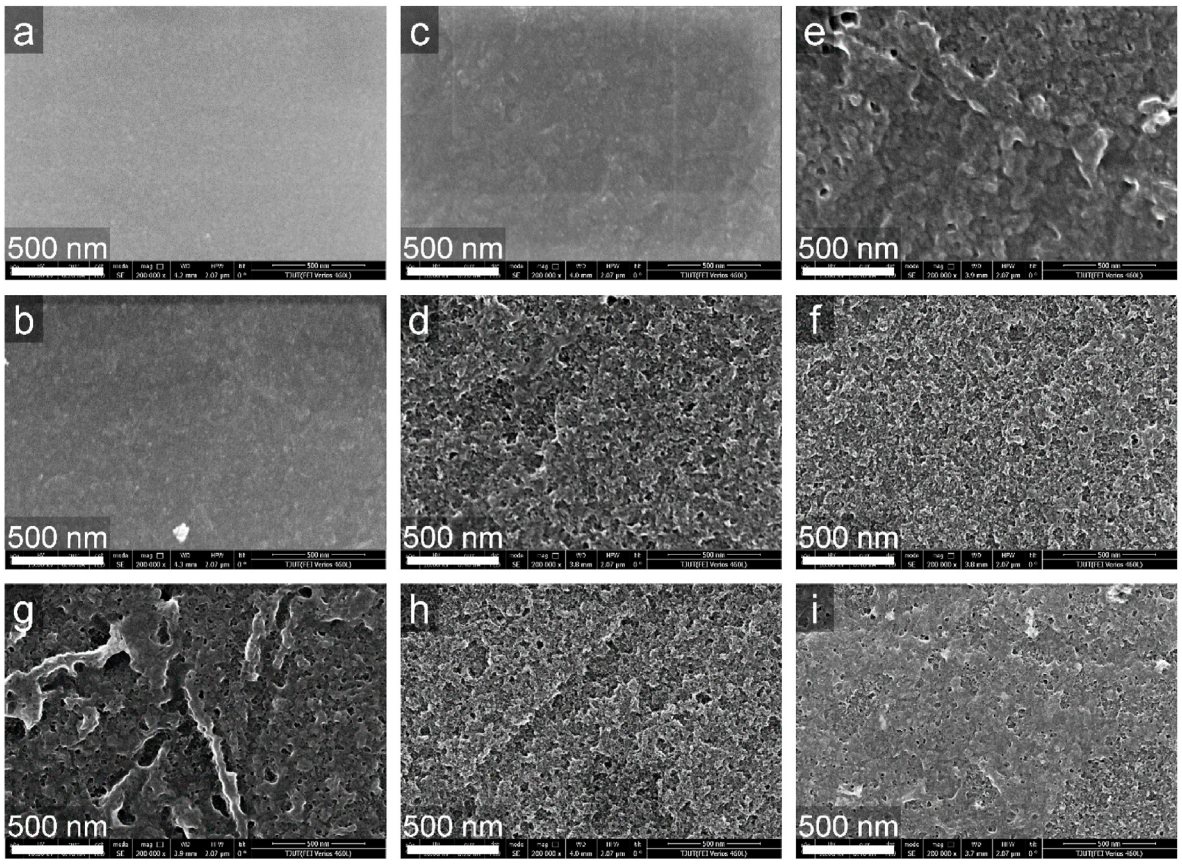

Fig. 1. FE-SEM images of (a) PAM, (b) Ni-PAM (NIP), (c, d) Ade-MIP before and after cleaning, (e, f) DA-MIP before and after cleaning, (g, h) dual-MIP before and after cleaning, and (i) 5 mA DA + dual-MIP.

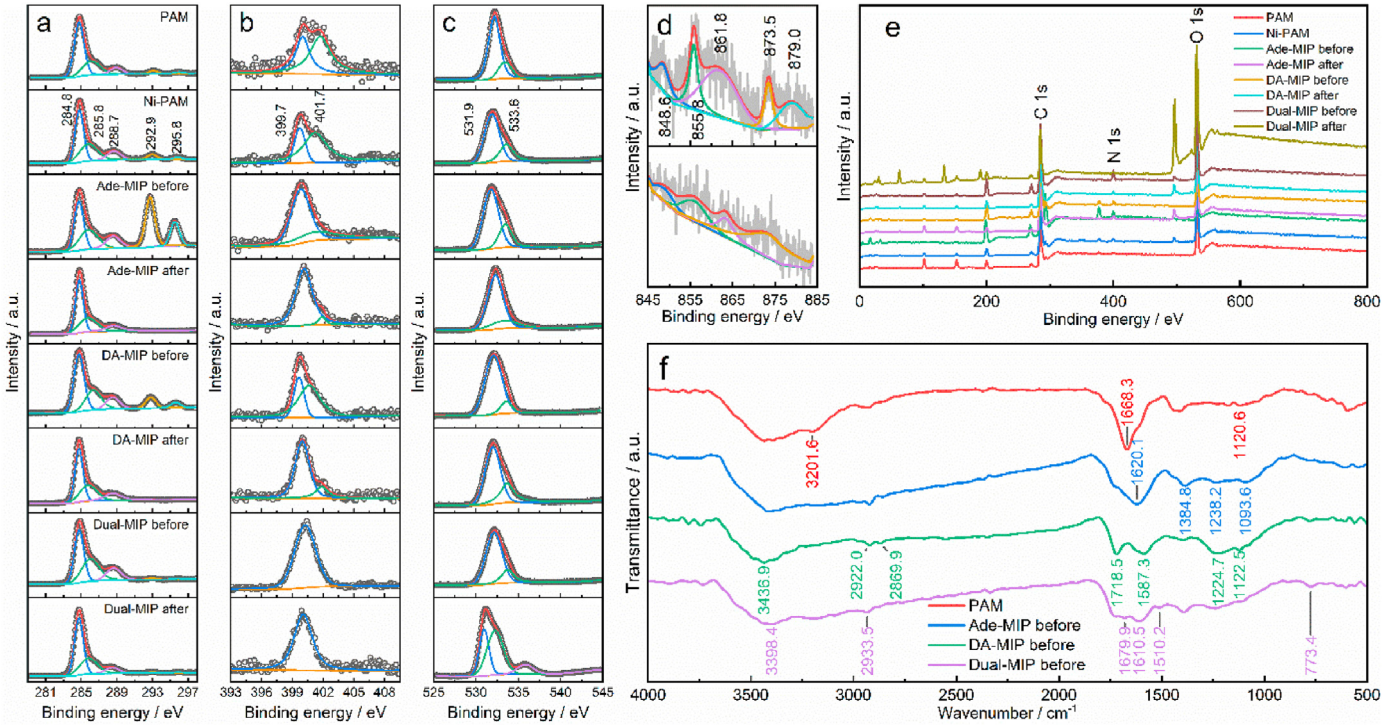

Fig. 2. (a–e) XPS: core-level C 1s, N 1s, O 1s, Ni 2p, and survey scan of PAM, Ni-PAM(NIP), Ade-MIP, DA-MIP, and dual-MIP electrodes before and after removing template molecules. (f) FTIR spectra of PAM, DA-PAM, Ade-PAM, and DA-Ade-PAM layers.

electrodes before and after the removal of the template molecules and observed that the thickness of the sensing films was reduced, indicating the successful removal of the imprinted templates.

For GCE, PAM/GCE, Ni-PAM(NIP)/GCE, DA-MIP, Ade-MIP, and dual-MIP, a series of CV curves were recorded at different potential scan rates ranging from 0.1 to 1 V s^{-1} (Fig. 3(b) and (c), and S4), and their Nyquist plots are shown in Fig. 3(d). The electrolyte was a mixture of 0.1 M KCl, 5 mM $K_4[Fe^{II}(CN)_6]$, and 5 mM $K_3[Fe^{III}(CN)_6]$. For all six electrodes, the peak potential was proportional to the logarithm of the scan rate (log v), while the peak current was proportional to the square root ($v^{1/2}$) of the scan rate (Fig. S5). The values of the effective electroactive surface area (A_{eff}) were calculated using the Randles-Sevcik equation ($I_p = 2.69 \times 10^5 n^{3/2} A_{eff} D_0^{1/2} c v^{1/2}$), where the number of electrons was $n = 1$, the concentration of probe molecules was $c = 5$ mM, the diffusion coefficient of $[Fe(CN)_6]^{4-/3-}$ was $D_0 = 7.6 \times 10^{-6}$ cm^2 s^{-1}, and the scan rate was $v = 0.01$–1 V; the $I_p/v^{1/2}$ value was equal to the slope in Fig. S3(b). In addition, the surface area of the MIP electrodes was calculated based on the results of the AFM measurements, and the ratio of the surface area/geometric area (A_S/A_G) was analyzed (Fig. 3(e)). Following the removal of the template molecules, the value of A_S/A_G increased, confirming the formation of imprinted holes (Fig. 3(e)). The PAM layer exhibited the highest A_{eff}/A_G ratio because of its strong electrolyte-adsorption capacity, while the A_{eff} value of the dual-MIP layer was 3.88 times that of A_G (Fig. 3(f)).

Figs. 3(d) and S6 show the Nyquist plots of the various electrodes. According to the equivalent circuit $R_s(C_1(R_{ct}(Q_1(R_1W_1))))(Q_2R_2)$ (inset in Fig. 3(d)) for GCE, PAM/GCE, NIP (Ni-PAM/GCE), DA-MIP, Ade-MIP, and dual-MIP, the charge transfer resistances of the electrolyte/electrode interfaces (R_{ct}) were ~13.73, ~1.54, ~2.31, ~3.42, ~3.63, and ~8.0 Ω, respectively (Fig. 3(g)). The R_{ct} values of PAM/GCE and Ni-PAM/GCE were substantially smaller than those of the bare GCE, indicating that the PAM matrix and Ni nanoparticles increased the rate of charge transfer through the adsorption of probe ions by the former and the improvement of conductivity of the sensitive layer by the latter. When MIP holes formed on the surface of Ni-PAM, the R_{ct} values increased: this may be related to the repulsion between imprinted

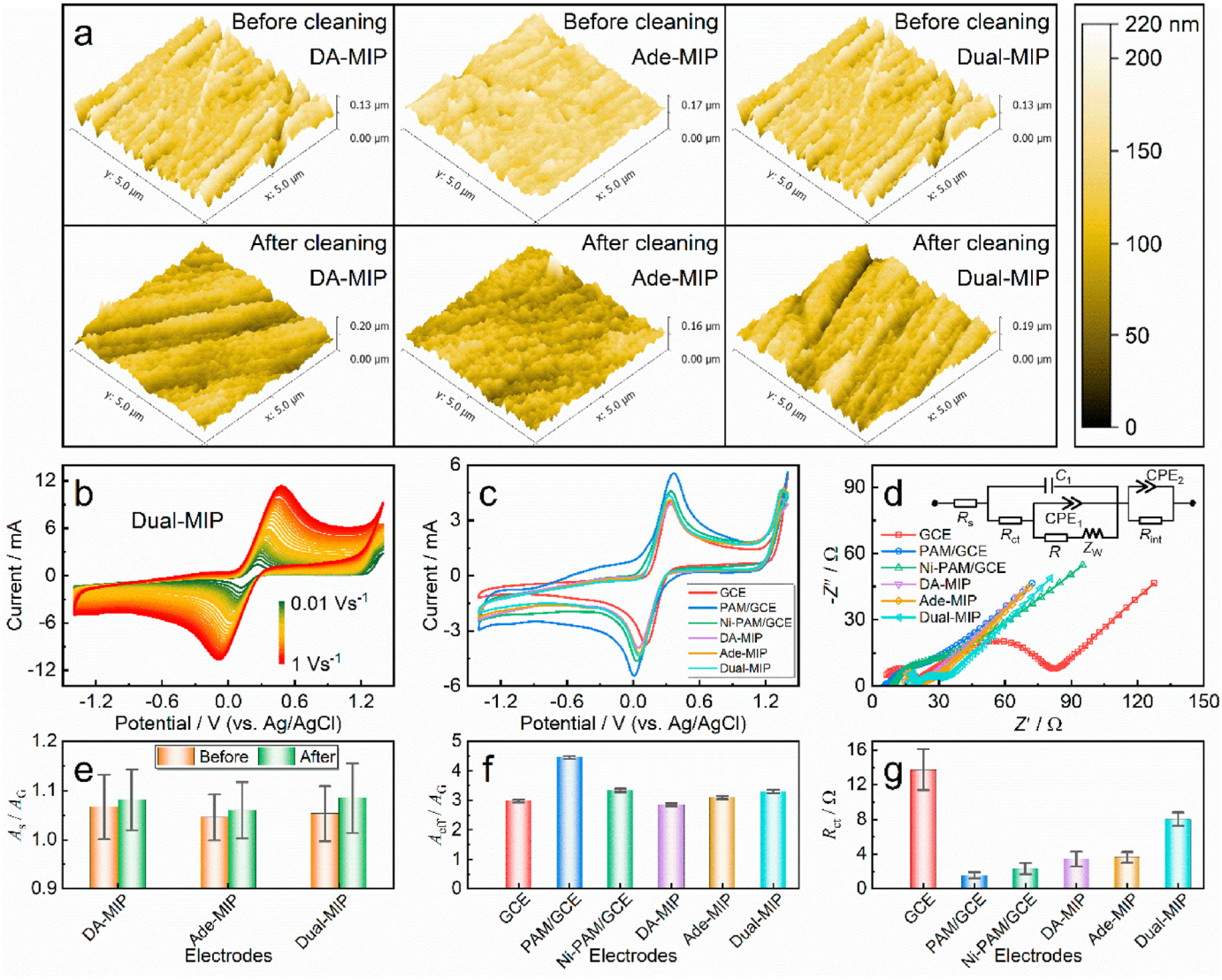

Fig. 3. (a) AFM images of DA-MIP, Ade-MIP, and dual-MIP electrodes before and after cleaning. (b) CV curves collected using dual-MIP/GCE at different scan rates (10–1000 mV s^{-1}). (c) CV curves of bare-, PAM-, Ni-PAM (NIP)-, Ade-MIP-, DA-MIP-, and dual-MIP/GCE electrodes at a scan rate of 100 mV s^{-1}. (d) Nyquist plots from the EIS measurements and the corresponding equivalent circuit. Electrolyte is a mixture of 0.1 M KCl, 5 mM $K_3[Fe(CN)_6]$, and 5 mM $K_4[Fe(CN)_6]$. (e) Relative surface areas. (f) Relative effective electroactive areas (A_{eff}). (g) Charge transfer resistance at electrolyte-electrode interface (R_{ct}).

holes and inorganic probe molecules, which increased the mass transfer resistance [48]. This confirms the formation of a large number of imprinted cavities.

3.4. Response analysis of sensitive components to DA and Ade

Fig. 4(a) shows the DPV responses of GCE, PAM/GCE, Ni-PAM/GCE (NIP), DA-MIP, Ade-MIP, and dual-MIP toward the electrocatalytic oxidation of DA and Ade. Two main oxidation peaks could be observed at ~0.12 V for DA and ~0.91 V for Ade (pH 7.4). In addition, the electroactive Ade oxidation products 2,8-oxoadenine (~0.37 V) and 2-oxoadenine (~0.62 V) formed on the electrode surface were detected [23]. Because of the large peak potential difference between DA and Ade (~0.8 V), the GCE and the modified electrodes were able separate them, although with different sensitivities. PAM and Ni nanoparticles, as components of the sensitive layer, did not modify the peak potentials of DA and Ade. The response capacities of dual-MIP and NIP electrodes for DA and Ade were compared. In the mixed solutions of DA and Ade (90 μM DA + 150 μM Ade; 30 μM DA + 30 μM Ade), the response currents of MIP sensor to DA were 1.7 (for 90 μM) and 2.4 (for 30 μM) times that of NIP sensor, and the peak currents of the former to Ade were 1.7 (for 150 μM) and 1.8 (for 30 μM) times that of the latter (Fig. S7).

Further, linear proportions were formed between the analyte concentration and the peak current at all electrodes (Fig. 4(b and c)). We compared the response sensitivities of the electrodes toward the two analytes in the concentration ranges of 0.1–90 μM for DA and 0.1–150 μM for Ade (Fig. 4(d)). Compared with the NIP responses to DA and Ade, the sensitivities of the dual-MIP sensor were significantly higher (Fig. 4(d)). In addition, the PAM and NIP did not exhibit higher sensitivity than the GCE toward DA and Ade. The NIP sensing membrane mainly relies on the electrocatalytic ability of the Ni-PAM layer to respond to DA and Ade, whereas the molecularly imprinted cavity plays a critical role in the Dual-MIP sensing layer. Therefore, the response of the MIP sensor to DA and Ade is superior to that of the NIP sensor.

In contrast, the sensitivity of DA-MIP was significantly higher than that of the three aforementioned electrodes (GCE, PAM-GCE, and NIP), indicating the successful molecular imprinting of DA. In addition, the DA-PAM layer exhibited a remarkably higher response sensitivity toward Ade, whereas Ade-MIP exhibited higher response sensitivity toward DA. Finally, the response sensitivities of the dual-MIP electrode toward DA and Ade were simultaneously higher.

3.5. Quantitative determination of DA and Ade using the dual-MIP sensor

The reliability of the dual-MIP sensor for the quantitative detection of DA and Ade was evaluated via three analysis methods:

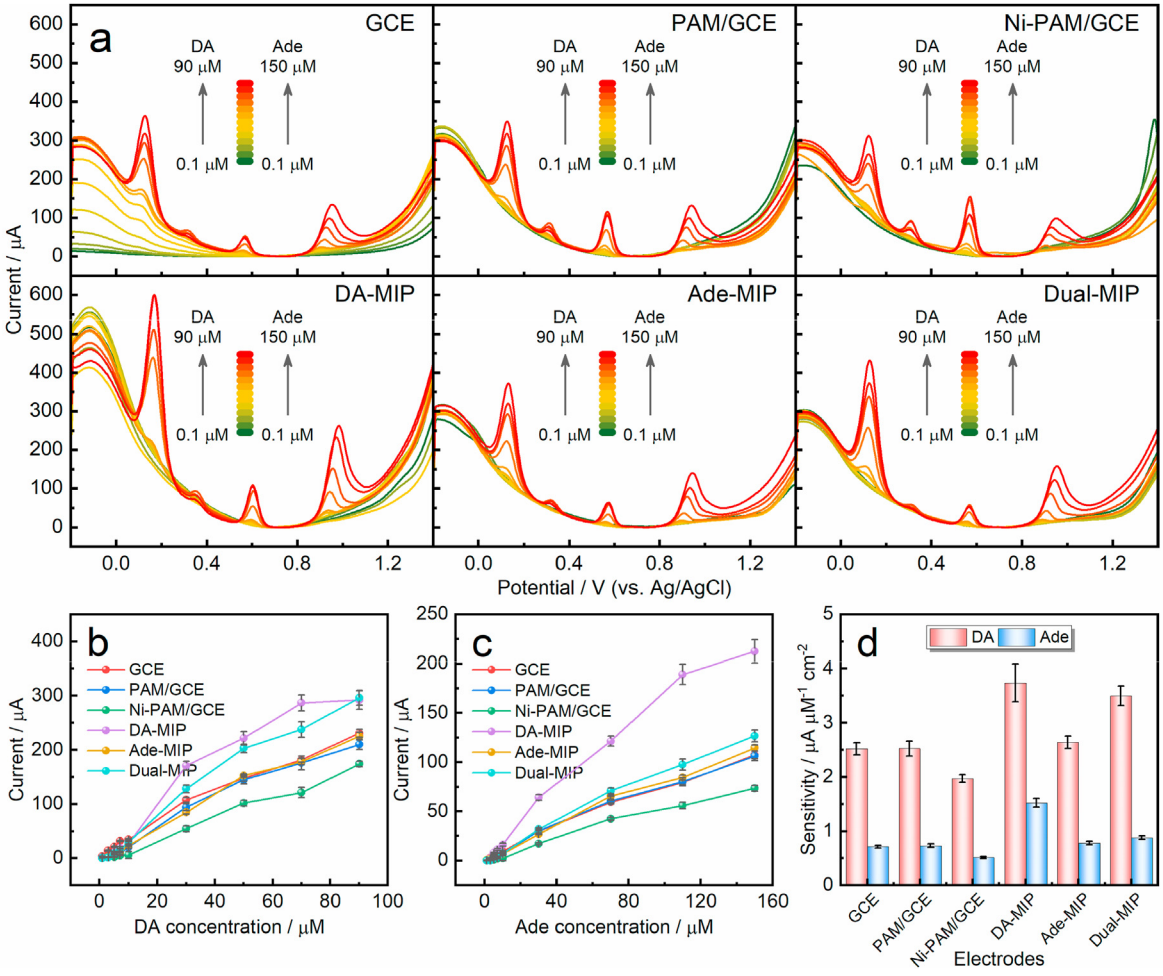

Fig. 4. (a) DPV curves recorded using GCE, PAM/GCE, Ni-PAM/GCE (NIP), DA-MIP, Ade-MIP, and dual-MIP electrodes in various mixed solutions of DA and Ade with pH 7.4 PBS as the supporting electrolyte. (b, c) Peak current as a function of DA (b) and Ade (c) concentrations. (c) Sensitivities toward DA and Ade.

separate detection, selective detection by varying the concentration of one analyte at a time, and simultaneous detection by varying the concentration of the two analytes simultaneously (Figs. 5(a) and 6(a)). The peak currents of DA and Ade increased gradually with increasing concentration from 0.1 to 200 μM (Fig. 5(b)). The sensitivity deviation between the three methods was lower than 10%, confirming the reliable quantitative response of the dual-MIP sensor to DA and Ade (Fig. 5(c)). The low interference between the signals from different species when using the dual-MIP sensor to detect DA and Ade resulted from the selection of separate, selective, and simultaneous detection methods.

Further, the adaptability of the dual-MIP sensor to different pH environments was evaluated in the pH range 5.0–9.0 (Fig. 6). The quantitative response to DA and Ade was achieved over the entire pH range investigated, indicating the excellent adaptability of this sensor (Fig. 6(a–c)). The peak potential difference between DA and Ade on the dual-MIP electrode is large in the pH range of 5.0–9.0, which indicates that the dual-MIP electrode has high selectivity and can effectively reduce the mutual interference between the two analytes. From the linear relationship between the pH and the peak potential (Fig. 6(d)), we calculated the response potentials for one pH unit as ~50 mV for DA and ~55 mV for Ade. This indicated that the transfer numbers of electrons and protons were approximately equal to those predicted by the Nernst equation (theoretically, 59 mV pH^{-1}). The corresponding electrochemical reactions are shown in Scheme 1(b).

In addition, a functional relationship was observed between the concentrations of DA and Ade and their respective peak currents (Fig. S8). Fig. 6(e and f) shows the sensitivities and limits of detection (LODs) of the dual-MIP sensor in response to DA and Ade at different pH values. The linear ranges, linear regression equations, and LODs are presented in Table S1. In general, the sensitivity toward DA decreased gradually with increase in pH, while that toward Ade increased (Fig. 6(e)). For the detection of DA, the sensitivity varied between 3.35 and 6.64 μA μM^{-1} in the low concentration range and between 0.39 and 2.48 μA μM^{-1} in the high concentration range. Taking pH 7.4 as example, for the ranges of DA concentrations 1–50 μM and 50–200 μM, the linear regression equations were $I = 4.18C_{DA}$ ($R^2 = 0.984$) and $I = 1.74\ C_{DA} + 124.40$ ($R^2 = 0.953$), respectively. In the pH range of 5.0–9.0, the LOD varied from 0.12 to 0.37 μM; at pH 7.4, its value was 0.27 μM. The LOD was calculated using the equation LOD = 3 s/b, where *s* is the standard deviation of 10 blanks (Fig. S9) and *b* is the slope of the calibration curve. For the response of Ade, the linear concentration range was different: 1–300 μM at pH 7.0 and 0.6–300 μM at pH 6.0. The sensitivity of Ade varied between 0.45 and 2.73 μA μM^{-1} with pH, with LODs ranging from 0.15 to 0.36 μM. Taking pH 7.4 again as example, for the Ade concentration range of 1–300 μM, the linear regression equation was $I = 0.8C_{Ade}$ ($R^2 = 0.997$), with the LOD being 0.28 μM.

A list of various DA and Ade electrochemical sensors, comparing their adaptive pH values, linear concentration ranges, sensitivities, and LODs, is provided in Table 1 [1,2,6,10,16,18,49–51]. In terms of pH adaptation, other sensors provide a single pH value, whereas the dual-MIP sensor has the advantage of a wide linear pH adaptation range of 5.0–9.0. In addition, in the range of our investigation, the lowest value of DA sensitivity was 0.023 μA μM^{-1} [51] and the highest value was 7.29 μA μM^{-1} [1], while the dual-MIP has a sensitivity of 0.39–6.64 μA μM^{-1}. The response sensitivity of DA is similar of superior to that of some sensors reported in the literature [2,16,51]. Several contemporary studies report Ade sensitivities in the range of 0.0118–10.87 μA μM^{-1}, whereas the sensitivity of the dual MIP sensor is 0.15–0.36 μA μM^{-1}, which is acceptable. The LODs of DA and Ade of previously reported sensors are in the ranges of 0.028–0.63 μM and 0.026–2.38 μM, respectively. In contrast, the LOD (0.12–0.37 μM) of the dual-MIP sensor for DA tends to be moderate; however, the LOD (0.15–0.36 μM) of Ade was remarkably low.

3.6. Repeatability, reproducibility, long-term stability, and anti-interference ability

A dual-MIP electrode was cleaned five times, and five DPV curves were recorded continuously each time, which did not exhibit large differences in peak current (Fig. S10). The DPV experiments were repeated in 0.1 M PBS (pH 7.4) containing 50 μM DA and 70 μM Ade for a total of 30 cycles (Fig. S11). The relative standard deviations (RSDs) of the response currents were 1.0% for DA and 1.1% for Ade (Fig. 7(a)). The batch-to-batch reproducibility of the fabrication procedure was also investigated (Fig. S12). Eight batches of modified sensors were constructed using the same preparation steps, and their reproducibility was tested in a mixture of 50 μM DA and 70 μM Ade, with RSDs of 3.37% and 3.27%, respectively, indicating the reliability of the preparation procedure

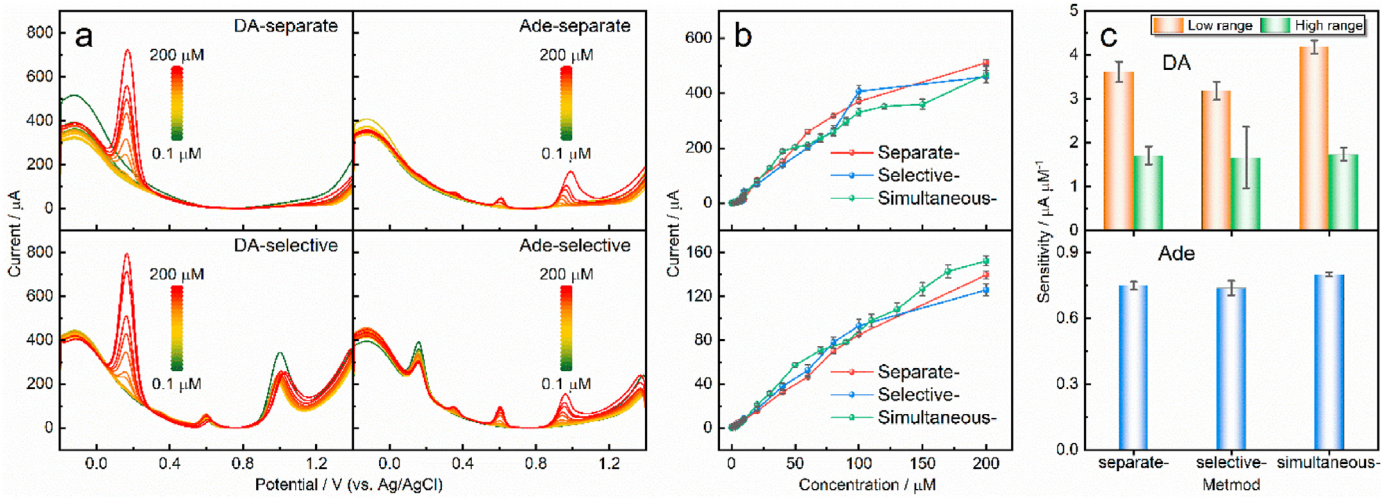

Fig. 5. Quantitative analysis of DA and Ade using the dual-MIP electrode. (a) DPV curves for individual and selective detection. (b) Peak current as a function of DA and Ade concentrations. (c) Sensitivities toward DA and Ade. The supporting electrolyte was a 0.1 M PBS solution (pH 7.4).

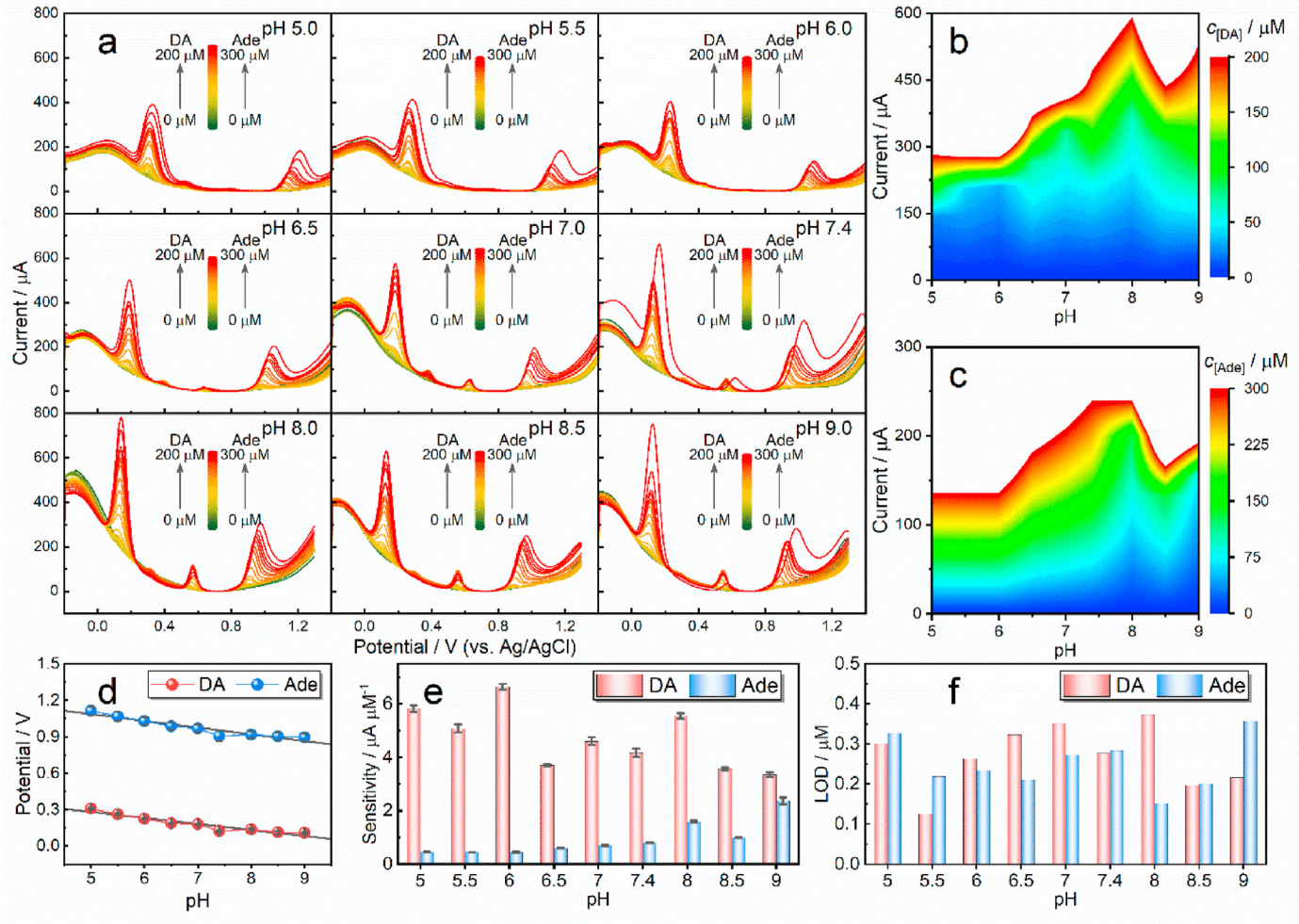

Fig. 6. Effect of pH on the quantitative analysis of the dual-MIP sensing electrode. (a) DPV curves recorded in 0.1 M PBS (pH 5.0–9.0) with mixtures of DA and Ade at various concentrations using the dual-MIP electrode. Peak current as a function of pH and (b) DA and (c) Ade concentrations. (d) Calibration plot of the peak potential as a function of pH. (e) Sensitivities toward DA and Ade. (f) LODs at various pH values.

Table 1
Comparison of the performance indicators of different electrochemical sensors for the detection of DA and Ade.

Sensor	pH range		Concentration range /μM		Sensitivity /μA μM^{-1}		Limit of detection /μM		Ref.
	DA	Ade	DA	Ade	DA	Ade	DA	Ade	
$FeTe_2$/GP	6.0	6.0	5–120	3–100	7.29	10.87	0.028	0.026	[1]
PImox-GO/GCE	3.0	3.0	12–278	9.6–215	0.211	0.232	0.63	1.28	[2]
PAD/IL-GR/MnO_2/GCE	–	4.0	–	10–300	–	0.0118	–	0.15	[6]
MoS_2-PGE	–	7.4	–	15–120	–	0.418	–	2.38	[10]
CuTRZMoO$_4$@PPY-2/GCE	2.5	–	1–100	–	0.1988	–	0.08	–	[16]
Au–ZnO NCAs/GF	7.5	–	0–80	–	4.36	–	0.04	–	[18]
SWCNH-NC/GCE	–	8.6	–	7.4–210	–	–	–	1.4	[49]
$Ni_{3-x}Te_2$/CPE	7.0	–	4–31	–	1.12	–	0.15	–	[50]
$K_2Fe_4O_7$/GCE	7.6	–	1–140	–	0.023	–	0.22	–	[51]
Dual-MIP	5.0–9.0	5.0–9.0	0.6–200	0.4–300	0.39–6.64	0.17–2.37	0.12–0.37	0.15–0.36	This work

(Fig. 7(b)). Moreover, in such a mixture, DA and Ade coexisted with interfering substances, such as 1–70 μM Cyt, 1–500 μM Glu, 5–70 μM AA, 1–90 μM Lys, 1–70 μM Tyr, 7–70 μM Gua, 7–50 μM UA, 1–10 μM Trp, 1–10 μM Ser, 0.1–50 μM Thy, 10–7000 μM K^+, 10–7000 μM Na^+, 10–5000 μM Ca^{2+}, 10–5000 μM Mg^{2+}, 10–3000 μM Cu^{2+}, 10–700 μM Zn^{2+}, 10–1000 μM Fe^{2+}, 10–3000 μM SO_4^{2-}, 10–500 μM SO_3^{2-}, and 10–700 μM CO_3^{2-}. Nevertheless, the sensors maintained a high current response to DA and Ade without apparent responses to the interfering substances; this indicates that the dual-MIP electrode possesses an excellent anti-interference property in the determination of DA and Ade (Table S2; Fig. 7(c), S13, and S14). Furthermore, the long-term

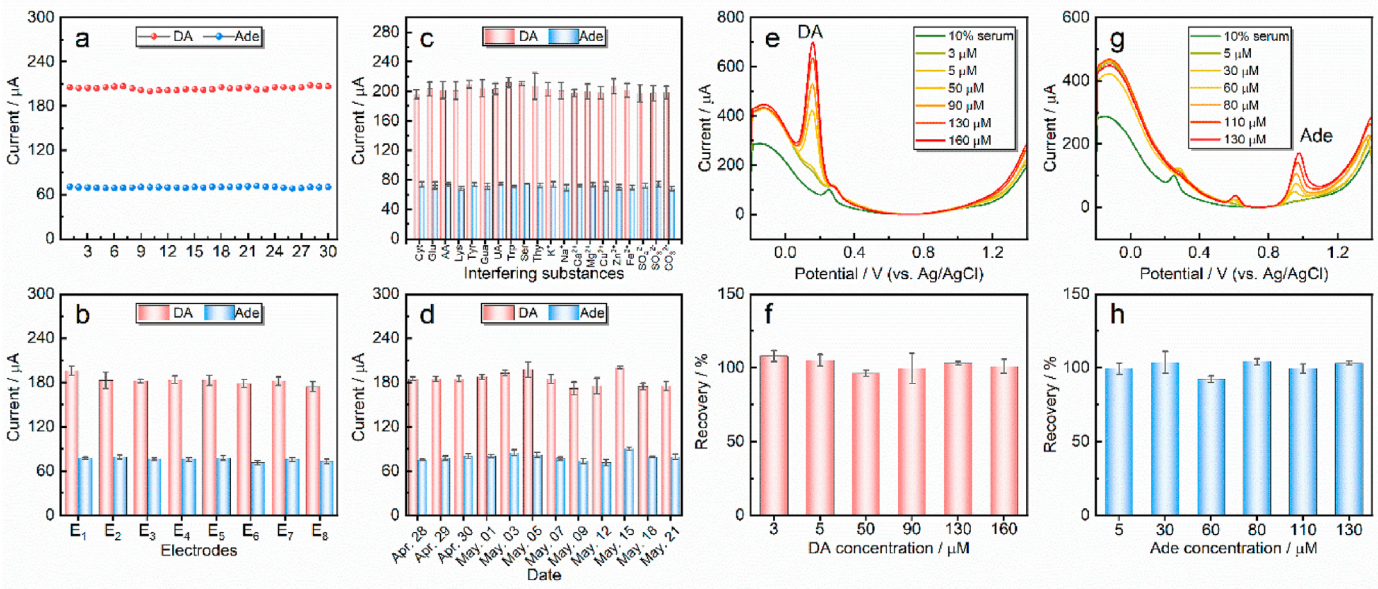

Fig. 7. (a) Peak currents of 50 μM DA and 70 μM Ade from 30 continuously recorded DPV curves. (b) Peak currents of DA and Ade recorded with eight electrodes in different batches. (c) anti-interference ability and (d) long-term stability. (e, g) DPV curves recorded in 10 vol% human serum solutions (pH 7.4) containing different concentrations of DA and Ade. (f, h) Recoveries of DA and Ade in serum.

stability of the sensor was investigated (Fig. S15). The results showed that the dual-MIP sensor was relatively stable for 4 w with an initial current response of 94.56% for DA and 105.66% for Ade (Fig. 7(d)).

3.7. Real sample assays

The applicability of the dual-MIP sensor was verified in human serum using the standard addition method. First, the serum was diluted 10 times with 0.1 M PBS (pH 7.4), and the concentrations of DA and Ade were measured. The diluted samples were then spiked with certain amounts of DA and Ade, which were determined through the DPV method shown in Fig. 7(e and f) using the dual-MIP sensor (Fig. S16). The corresponding analytical results and recoveries are presented in Table S3 and Fig. 7(g and h). The recoveries were in the range of 96%–108% for DA and 92%–104% for Ade, indicating that the dual-MIP sensor can be reliably used for detecting DA and Ade in real samples.

4. Conclusion

Dopamine (DA) and adenine (Ade) are generally detected synchronously in body fluids because their levels can be used for comprehensive early monitoring of human nervous and immune system diseases. A dual-response Ni-PAM-based MIP electrochemical biosensor was constructed for the simultaneous detection of DA and Ade. Firstly, a dual-MIP sensitive layer was assembled through the Ni-assisted electro-polymerization of AM. This is the first report on this type of procedure, which is suitable for depositing solid molecularly imprinted polymer films on the surfaces of various basic electrodes. Secondly, the dual-MIP sensor underwent exhaustive characterization, which revealed its excellent electrocatalytic activity, a high A_{eff}/A_G ratio of 3.88, and a low charge transfer resistance at the electrolyte/electrode interface of ~8.0 Ω. Furthermore, compared to the GCE and NIP sensors, the dual-MIP sensing electrode exhibited significantly higher response sensitivities toward DA and Ade. Because the components of the imprinted membrane have relatively weak electrocatalytic activities for DA and Ade, the imprinted cavity plays a critical role, effectively inhibiting the interference between the two analytes. Because of operating on the MIP detection mechanism, the sensor exhibited high specificity for DA and Ade, which improved the reliability of the quantitative detection model. Finally, a series of quantitative detection models were established in a wide pH range (5.0–9.0), highlighting the suitability of this sensor for the quantitative analysis of DA and Ade in various body fluids such as cell fluid, blood, and urine. Further research will explore the feasibility of this novel strategy, based on the electrochemical molecular imprinting of an Ni-PAM matrix, in the construction of electrochemical sensing layers with potential application in the analysis of a wider variety of biomolecules.

CRediT authorship contribution statement

Tianrun Zhang: Conceptualization, Methodology. **Xiuwei Xuan:** Formal analysis, Data curation, Software. **Mingji Li:** Investigation, Writing – original draft, preparation, Supervision. **Cuiping Li:** Formal analysis. **Penghai Li:** Formal analysis. **Hongji Li:** Writing – review & editing, Writing – original draft, preparation.

Declaration of competing interest

The authors declare that they have no known competing financial interests or personal relationships that could have appeared to influence the work reported in this paper.

Acknowledgements

This work was supported by the Natural Science Foundation of Tianjin City (No. 20JCZDJC00290).

Appendix A. Supplementary data

Supplementary data to this article can be found online at https://doi.org/10.1016/j.aca.2022.339689.

References

[1] S. Pradhan, S. Pramanik, D.K. Das, R. Bhar, R. Bandyopadhyay, P. Millner, et al., Nanosized iron telluride for simultaneous nanomolar voltammetric determination of dopamine, uric acid, guanine and adenine, New J. Chem. 43 (2019) 10590–10600.

[2] X. Liu, L. Zhang, S. Wei, S. Chen, X. Ou, Q. Lu, Overoxidized polyimidazole/graphene oxide copolymer modified electrode for the simultaneous determination of ascorbic acid, dopamine, uric acid, guanine and adenine, Biosens. Bioelectron. 57 (2014) 232–238.

[3] J. Yang, Y. Hu, Y. Li, Molecularly imprinted polymer-decorated signal on-off ratiometric electrochemical sensor for selective and robust dopamine detection, Biosens. Bioelectron. 135 (2019) 224–230.

[4] Y. Wang, K. Kang, S. Wang, W. Kang, C. Cheng, L.M. Niu, et al., A novel label-free fluorescence aptasensor for dopamine detection based on an Exonuclease III- and SYBR Green I- aided amplification strategy, Sensor. Actuator. B Chem. 305 (2020) 127348.

[5] A. Perebikovsky, A.T. Hwu, A.R. Yale, M. Ghazinejad, M. Madou, Nanofibrous carbon multifunctional smart scaffolds for simultaneous cell differentiation and dopamine detection, ACS Biomater. Sci. Eng. 6 (2020) 225–234.

[6] S. Zhang, X.M. Zhuang, D.D. Chen, F. Luan, T. He, C.Y. Tian, et al., Simultaneous voltammetric determination of guanine and adenine using MnO_2 nanosheets and ionic liquid-functionalized graphene combined with a permeation-selective polydopamine membrane, Microchim. Acta 186 (2019) 450.

[7] K. Prusty, A. Biswal, S.B. Biswal, S.K. Swain, Synthesis of soy protein/polyacrylamide nanocomposite hydrogels for delivery of ciprofloxacin drug, Mater. Chem. Phys. 234 (2019) 378–389.

[8] L. Zhang, J. Zhang, Multiporous molybdenum carbide nanosphere as a new charming electrode material for highly sensitive simultaneous detection of guanine and adenine, Biosens. Bioelectron. 110 (2018) 218–224.

[9] B.N. Mao, L.T. Qian, M. Govindhan, Z.G. Liu, A.C. Chen, Simultaneous electrochemical detection of guanine and adenine using reduced graphene oxide decorated with AuPt nanoclusters, Microchim. Acta 188 (2021) 276.

[10] N. Vishnu, S. Badhulika, Single step grown MoS_2 on pencil graphite as an electrochemical sensor for guanine and adenine: a novel and low cost electrode for DNA studies, Biosens. Bioelectron. 124 (2019) 122–128.

[11] W. Zheng, K.-H. Yoo, A.M. Abd El-Aty, D.-H. Park, J.-M. Choi, S.-K. Kim, et al., Quantitative determination of carbasalate calcium derived metabolites, acetylsalicylic acid and salicylic acid, in six animal foods using liquid-liquid extraction method coupled with liquid chromatography-tandem mass spectrometry, Food Chem. 278 (2019) 744–750.

[12] Y. Zhang, W. Ren, Y.Z. Fan, H.Q. Luo, N.B. Li, Chemically-modulated turn-on fluorescence for rapid and visual discrimination of norepinephrine and epinephrine and its application for dopamine-beta-hydroxylase detection, Sensor. Actuator. B Chem. 305 (2020) 127463.

[13] M. Zhao, L. Bai, W. Cheng, X. Duan, H. Wu, S. Ding, Monolayer rubrene functionalized graphene-based eletrochemiluminescence biosensor for serum cystatin C detection with immunorecognition-induced 3D DNA machine, Biosens. Bioelectron. 127 (2019) 126–134.

[14] J. Qin, S. Gao, H. Li, C. Li, M. Li, Growth of monolayer and multilayer graphene on glassy carbon electrode for simultaneous determination of guanine, adenine, thymine, and cytosine, J. Electroanal. Chem. 895 (2021) 115403.

[15] N. Ahmadi, M. Bagherzadeh, A. Nemati, Comparison between electrochemical and photoelectrochemical detection of dopamine based on titania-ceria-graphene quantum dots nanocomposite, Biosens. Bioelectron. 151 (2020) 111977.

[16] K. Zhou, D. Shen, X. Li, Y. Chen, L. Hou, Y. Zhang, et al., Molybdenum oxide-based metal-organic framework/polypyrrole nanocomposites for enhancing electrochemical detection of dopamine, Talanta 209 (2020) 120507.

[17] X. Zhao, Y. Cui, Y. He, S. Wang, J. Wang, Synthesis of multi-mode quantum dots encoded molecularly imprinted polymers microspheres and application in quantitative detection for dopamine, Sensor. Actuator. B Chem. 304 (2020) 127265.

[18] H.Y. Yue, H.J. Zhang, S. Huang, X.X. Lu, X. Gao, S.S. Song, et al., Highly sensitive and selective dopamine biosensor using Au nanoparticles-ZnO nanocone arrays/graphene foam electrode, Mater. Sci. Eng. C 108 (2020) 110490.

[19] Z. Yang, M. Li, H. Li, H. Li, C. Li, B. Yang, Polycrystalline boron-doped diamond-based electrochemical biosensor for simultaneous detection of dopamine and melatonin, Anal. Chim. Acta 1135 (2020) 73–82.

[20] A. Şenocak, S.O. Tümay, İ. Ömeroğlu, V. Şanko, Crosslinker polycarbazole supported magnetite MOF@CNT hybrid material for synergetic and selective voltammetric determination of adenine and guanine, J. Electroanal. Chem. 905 (2022) 115963.

[21] L.F. Ji, S. Yu, X. Zhou, Y.K. Bao, F.C. Yang, W.D. Kang, et al., Modification of electron structure on the semiconducting single-walled carbon nanotubes for effectively electrosensing guanine and adenine, Anal. Chim. Acta 1079 (2019) 86–93.

[22] A.V. Papavasileiou, M.G. Trachioti, J. Hrbac, M.I. Prodromidis, Simultaneous determination of guanine and adenine in human saliva with graphite sparked screen-printed electrodes, Talanta 239 (2022) 123119.

[23] A.M. Oliveira-Brett, V. Diculescu, J.A.P. Piedade, Electrochemical oxidation mechanism of guanine and adenine using a glassy carbon microelectrode, Bioelectrochemistry 55 (2002) 61–62.

[24] X. Bai, B. Zhang, M. Liu, X. Hu, G. Fang, S. Wang, Molecularly imprinted electrochemical sensor based on polypyrrole/dopamine@graphene incorporated with surface molecularly imprinted polymers thin film for recognition of olaquindox, Bioelectrochemistry 132 (2020) 107398.

[25] M. You, S. Yang, Y. An, F. Zhang, P. He, A novel electrochemical biosensor with molecularly imprinted polymers and aptamer-based sandwich assay for determining amyloid-β oligomer, J. Electroanal. Chem. 862 (2020) 114017.

[26] C. Salvo-Comino, I. Rassas, S. Minot, F. Bessueille, M.L. Rodriguez-Mendez, A. Errachid, et al., Voltammetric sensor based on electrodeposited molecularly imprinted chitosan film on BDD electrodes for catechol detection in buffer and in wine samples, Mater. Sci. Eng. C 110 (2020) 110667.

[27] Y.Y. Yang, Y.T. Li, X.J. Li, L. Zhang, E.K. Fodjo, S. Han, Controllable in situ fabrication of portable AuNP/mussel-inspired polydopamine molecularly imprinted SERS substrate for selective enrichment and recognition of phthalate plasticizers, Chem. Eng. J. 402 (2020) 125179.

[28] R. Shariati, B. Rezaei, H.R. Jamei, A.A. Ensafi, Manufacturing of a sensitive and selective optical sensor based on molecularly imprinted polymers and green carbon dots synthesized from cedrus plant for trace analysis of propranolol, Anal. Sci. 35 (2019) 1083–1088.

[29] Y. Wu, P. Deng, Y. Tian, Z. Ding, G. Li, J. Liu, et al., Rapid recognition and determination of tryptophan by carbon nanotubes and molecularly imprinted polymer-modified glassy carbon electrode, Bioelectrochemistry 131 (2020) 107393.

[30] J. Zhang, X.-T. Guo, J.-P. Zhou, G.-Z. Liu, S.-Y. Zhang, Electrochemical preparation of surface molecularly imprinted poly(3-aminophenylboronic acid)/MWCNTs nanocomposite for sensitive sensing of epinephrine, Mater. Sci. Eng. C 91 (2018) 696–704.

[31] L.F. Pompeu Prado Moreira, E. Buffon, N.R. Stradiotto, Electrochemical sensor based on reduced graphene oxide and molecularly imprinted poly(phenol) for D-xylose determination, Talanta 208 (2020) 120379.

[32] C. Malitesta, E. Mazzotta, R.A. Picca, A. Poma, I. Chianella, S.A. Piletsky, MIP sensors – the electrochemical approach, Anal. Bioanal. Chem. 402 (2012) 1827–1846.

[33] S. Garg, T. Bal, S.G. Panpalia, A.D. Rajora, B.D. Ghosh, Preparation and characterization of microwave irradiated pH-sensitive polyacrylamide grafted flax seed mucilage graft copolymeric hydrogel (PFLSM-g-PAM-cl-MBA) and its evaluation as effective polymeric scaffold, Sustain. Chem. Pharm. 22 (2021) 100479.

[34] K. Prusty, S.K. Swain, Release of ciprofloxacin drugs by nano gold embedded cellulose grafted polyacrylamide hybrid nanocomposite hydrogels, Int. J. Biol. Macromol. 126 (2019) 765–775.

[35] P. Chaudhary, D.K. Maurya, S. Sikarwar, B.C. Yadav, G.I. Dzhardimalieva, R. Prakash, Development of nanostructured nickel reinforced polyacrylamide via frontal polymerization for a reliable room temperature humidity sensor, Eur. Polym. J. 112 (2019) 161–169.

[36] S. Rudenja, N. Zhao, S. Liu, Surface interpenetrating networks of polyacrylamide in poly(ethylene terephthalate) as a means of surface modification, Eur. Polym. J. 46 (2010) 2078–2084.

[37] Y. He, S. Gou, L. Zhou, L. Tang, T. Liu, L. Liu, et al., Amidoxime-functionalized polyacrylamide-modified chitosan containing imidazoline groups for effective removal of Cu^{2+} and Ni^{2+}, Carbohydr. Polym. 252 (2021) 117160.

[38] L. Ndlwana, M.M. Motsa, B.B. Mamba, A unique method for dopamine-cross-linked graphene nanoplatelets within polyethersulfone membranes (GNP-pDA/PES) for enhanced mechanochemical resistance during NF and RO desalination, Eur. Polym. J. 136 (2020) 109889.

[39] Z. Zhao, Y. Huang, Y. Wu, S. Li, H. Yin, J. Wang, α-ketoglutaric acid modified chitosan/polyacrylamide semi-interpenetrating polymer network hydrogel for removal of heavy metal ions, Colloids Surf., A 628 (2021) 127262.

[40] J.A. Behan, F. Grajkowski, D.R. Jayasundara, L. Vilella-Arribas, M. García-Melchor, P.E. Colavita, Influence of carbon nanostructure and oxygen moieties on dopamine adsorption and charge transfer kinetics at glassy carbon surfaces, Electrochim. Acta 304 (2019) 221–230.

[41] S.D. Rani, R. Ramachandran, S. Sheet, M.A. Aziz, Y.S. Lee, A.G. Al-Sehemi, et al., $NiMoO_4$ nanoparticles decorated carbon nanofiber membranes for the flexible and high performance glucose sensors, Sensor. Actuator. B Chem. 312 (2020) 127886.

[42] Y. Liu, Y. Zheng, Q. Xu, Y. Shi, Z. Tian, R. wang, et al., Controllable synthesis of $NiSe/MoSe_2/MoO_2$ 3D hierarchical hollow microspheres with enhanced performance for asymmetric supercapacitors, Chem. Eng. J. 387 (2020) 124121.

[43] A. Savk, K. Cellat, K. Arikan, F. Tezcan, S.K. Gulbay, S. Kizildag, et al., Highly monodisperse Pd-Ni nanoparticles supported on rGO as a rapid, sensitive, reusable and selective enzyme-free glucose sensor, Sci. Rep. 9 (2019) 19228.

[44] B. Singh, M. Mohan, B. Singh, Synthesis and characterization of the azadirachta indica gum–polyacrylamide interpenetrating network for biomedical applications, Carbohydr. Polym. Technol. Appl. 1 (2020) 100017.

[45] S.S. Ngema, A.K. Basson, T.S. Maliehe, Synthesis, characterization and application of polyacrylamide grafted bioflocculant, Phys. Chem. Earth, Parts A/B/C 115 (2020) 102821.

[46] J. Chen, S.-L. Liu, W. Feng, X.-J. Bao, F.-L. Yang, The influence of Fe^{2+} doping on the microstructure and photochromic behavior of polyoxometalates acid/polyacrylamide hybrid films, Opt. Mater. 35 (2013) 973–977.

[47] T.A. Mohamed, I.A. Shabaan, W.M. Zoghaib, J. Husband, R.S. Farag, A.E.-N.M.A. Alajhaz, Tautomerism, normal coordinate analysis, vibrational assignments, calculated IR, Raman and NMR spectra of adenine, J. Mol. Struct. 938 (2009) 263–276.

[48] X.X. Xiong, C. Li, X.Y. Yang, Y. Shu, D.Q. Jin, Y. Zang, et al., In situ grown TiO_2

nanorod arrays functionalized by molecularly imprinted polymers for salicylic acid recognition and detection, J. Electroanal. Chem. 873 (2020) 114394.
[49] T.S. Ortolani, T.S. Pereira, M.H.M.T. Assumpção, F.C. Vicentini, G. Gabriel de Oliveira, B.C. Janegitz, Electrochemical sensing of purines guanine and adenine using single-walled carbon nanohorns and nanocellulose, Electrochim. Acta 298 (2019) 893–900.
[50] K. de Fatima Ulbrich, J.P. Winiarski, C.L. Jost, C.E. Maduro de Campos, Mechanochemical synthesis of a $Ni_{3-x}Te_2$ nanocrystalline composite and its application for simultaneous electrochemical detection of dopamine and adrenaline, Composites, Part B 183 (2020) 107649.
[51] X. Sun, L. Zhang, X. Zhang, X. Liu, J. Jian, D. Kong, et al., Electrochemical dopamine sensor based on superionic conducting potassium ferrite, Biosens. Bioelectron. 153 (2020) 112045.